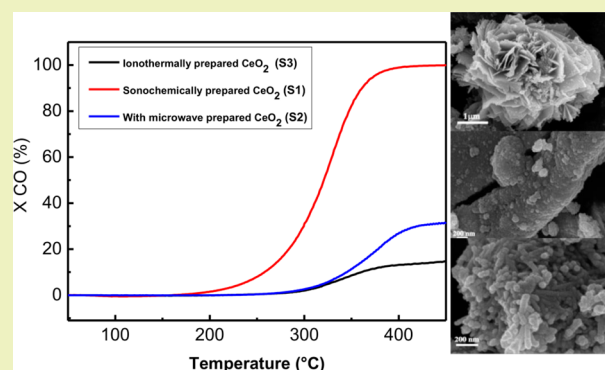


Ionic Liquid-Assisted Sonochemical Preparation of CeO₂ Nanoparticles for CO OxidationTarek Alammar,[†] Heshmat Noei,[‡] Yuemin Wang,[§] Wolfgang Grünert,[§] and Anja-Verena Mudring^{*,†,||}[†]Ruhr-Universität Bochum, Inorganic Chemistry III-Materials Engineering and Characterization, D-44780 Bochum, Germany[‡]Deutsches Elektronen Synchrotron DESY, D-22607 Hamburg, Germany[§]Ruhr-Universität Bochum, Laboratory of Industrial Chemistry, D-44780 Bochum, Germany^{||}Materials Science and Engineering, Iowa State University and Critical Materials Institute, Ames Laboratory, Ames, Iowa 50011, United States

S Supporting Information

ABSTRACT: CeO₂ nanoparticles were synthesized via a one-step ultrasound synthesis in different kinds of ionic liquids based on bis(trifluoromethanesulfonylamide, [Tf₂N]⁻, in combination with various cations including 1-butyl-3-methylimidazolium ([C₄mim]⁺), 1-ethyl-2,3-dimethylimidazolium ([Edimim]⁺), butyl-pyridinium([Py₄]⁺), 1-butyl-1-methyl-pyrrolidinium ([Pyr₁₄]⁺), and 2-hydroxyethyl-trimethylammonium ([N₁₁₁₂OH]⁺). Depending on synthetic parameters, such as ionic liquid, Ce(IV) precursor, heating method, and precipitator, formed ceria exhibits different morphologies, varying from nanospheres, nanorods, nanoribbons, and nanoflowers. The morphology, crystallinity, and chemical composition of the obtained materials were characterized by scanning electron microscopy (SEM), X-ray diffraction (XRD), X-ray photoelectron spectroscopy (XPS), energy dispersive X-ray spectroscopy (EDX), Raman spectroscopy, and N₂ adsorption. The structural and electronic properties of the as-prepared CeO₂ samples were probed by CO adsorption using IR spectroscopy under ultrahigh vacuum conditions. The catalytic activities of CeO₂ nanoparticles were investigated in the oxidation of CO. CeO₂ nanospheres obtained sonochemically in [C₄mim][Tf₂N] exhibit the best performance for low-temperature CO oxidation. The superior catalytic performance of this material can be related to its mesoporous structure, small particle size, large surface area, and high number of surface oxygen vacancy sites.

KEYWORDS: Catalysis, Ceria, CO oxidation, Ionic liquids, Nanomaterials



INTRODUCTION

Rare earth metal oxides, especially cerium oxide, have been a topic of interest to researchers in different fields owing to applications in solid oxide fuel cell anodes, as a catalyst in the three-way automobile exhaust system, as an oxygen storage capacitor, UV blocker and filters, efficient polishing agent for glasses, hybrid solar cells, high refractive index materials, coatings for corrosion protection of metals and alloys, cosmetics, ceramics, and in phosphors, where cerium is one of the most important constituent in several of the new generation of phosphors in tricolor lamps.^{1–6} Cerium(IV) oxide as a wide band gap semiconducting material (~3.2 eV) can absorb light in the near UV region and slightly in the visible region and has therefore been regarded as a promising material for photocatalysis, especially when brought to the nanoscale. However, it is well known that important physical and chemical properties such as the band gap of CeO₂ nanoparticles can be quite different from the bulk. Their properties rely mainly on the morphology, size, and dimensions. Hence, considerable

effort has been dedicated to prepare CeO₂ nanoparticles with controlled shape such as nanoplates, nanotubes, shuttle-shaped, nanorods, nanowires, and flower-like using different methods such as hydrothermal synthesis,^{7–9} solvothermal,^{10,11} thermal decomposition,¹² microwave-assisted hydrothermal,¹³ sol-gel process,¹⁴ mechanochemical processing,¹⁵ and gas condensation.¹⁶ These methods all have certain drawbacks as they either use high pressure or high temperatures and expensive raw materials such as surface capping agents or organic solvents. Therefore, improving and exploring a new technique to prepare the size and shape-controlled ceria, which relies on a simple approach to reduce the cost of production using environmentally benign reagents and mild preparation conditions, is desirable. In that context, the exploration of ionic liquids for synthesis appears to be beneficial. Ionic liquids are salts

Received: July 26, 2014

Revised: September 19, 2014

Published: October 10, 2014

composed of only ions that are liquid at relatively low temperatures (below 100 °C). Ionic liquids (ILs) have received substantial attention for materials synthesis in recent years because of their special properties. The possibility to vary the cation and anion as well as the ion combination makes it possible to engineer a solvent with unique properties such as high ion mobility, low melting point, negligible vapor pressure, good thermal stability, low toxicity, large electrochemical window, nonflammability, and the ability to dissolve a variety of chemicals in a highly polar yet weakly coordinating solvent.^{17,18} Recently, we were able to show that the combination of ionic liquids with ultrasound is a powerful method when it comes to the synthesis of nanooxides.^{19–22}

Sonochemistry, albeit mostly in conventional and volatile solvents, has attracted increasing interest of many researchers over the past decade for the synthesis of inorganic nanostructured materials. The chemical effects of ultrasound originate from acoustic cavitation,²³ which occurs in several stages involving the steps of nucleation, growth, and collapse of bubbles in the liquid. The collapse of the bubbles provokes extreme conditions; high temperatures up to 5000 °C and high pressures of about 500 atm can be reached.²⁴ Yet sonochemical synthesis has the advantage that it is experimentally comparatively simple.

We have employed sonochemistry for the synthesis of nano-CeO₂ in ionic liquids. Here, the ionic liquid can act not only as the solvent but also as the structure directing agent. Aside from a variation of the ionic liquid, the influences of the synthesis conditions such as conversion method, precipitator, irradiation time, and Ce precursor on the morphology, size, and the catalytic activity toward CO oxidation were investigated in detail.

■ EXPERIMENTAL SECTION

Materials. All reagents employed were commercially available and directly used without further purification. All the ILs used in this study were synthesized according to the literature.^{25,26} Lithium bis(trifluoromethylsulfanyl)amide (99%), butylpyridiniumbis(trifluoromethylsulfanyl)amide (99%), and 1-butyl-1-methylpyrrolidinium chloride (99%) were purchased from Iolitec; 1-ethyl-2,3-dimethylimidazolium chloride from Merck; and 1-chlorobutane (99%), ethanol (p.a.), and 1-methylimidazole from Sigma-Aldrich. Choline chloride (99%) was from Acros; cerium(III) acetate hydrate (99%) and cerium(III) chloride hydrate (99%) were from ABCR. Sodium hydroxide (98%) and ammonium hydroxide (33%) were from J.T. Baker, and cerium(III) nitrate hexahydrate (99%) was from Alfa-Aesar. The nano-CeO₂ materials were compared with a microcrystalline CeO₂, which was purchased from Sigma-Aldrich and is labeled M-CeO₂.

Experimental Procedures. In a typical synthesis, 0.2 g of cerium(III) acetate monohydrate was added to 0.1 g of sodium hydroxide and 2 mL of the respective bis(trifluoromethylsulfanyl)amide IL with either 1-ethyl-2,3-dimethylimidazolium ([Edimim]⁺), butyl-pyridinium ([Py₄]⁺), 1-butyl-1-methyl-pyrrolidinium ([Pyr₁₄]⁺), or 2-hydroxyethyl-trimethylammonium ([N₁₁₁₂OH]⁺) as the cation. The reaction mixture was then stirred for 30 min.

For the sonochemical synthesis, a commercial ultrasound bath (USC200T, VWR International, 45 kHz and 60 W) was used. The reaction mixtures were placed in glass tubes with a screw top and then irradiated in an ultrasound bath for 12 h under ambient conditions. The product was separated by centrifugation for 5 min at 2000 rpm, washed thoroughly with ethanol and distilled water, and dried overnight in the air at 80 °C (yield: 85%).

To explore the effect of the precipitating agent on the product, we used an aqueous solution of NH₄OH under otherwise similar conditions. The samples were also prepared by using different Ce

sources such as cerium(III) nitrate hydrate and cerium(III) chloride hydrate.

For the microwave synthesis, the reaction mixture was placed in 10 mL glass vessels equipped with a Teflon septum and irradiated for 10 min at 80 °C using a single-mode microwave operating at 2455 MHz (CEM Discover, Kamp Lintfort, D). The reaction time, temperature, and irradiation power were computer controlled. The sample was then allowed to cool to room temperature, and the product was separated by centrifugation for 5 min at 2000 rpm, washed thoroughly with ethanol and distilled water, and dried overnight in the air at 80 °C (yield: 79%). Finally, the dried solid was calcined in air at 425 °C for 4 h.

Isothermal experiments were performed in 50 mL Teflon cups enclosed in stainless steel autoclaves (Parr Instrument, U.S.A.). The reaction mixture was transferred to a Teflon cup and sealed in the autoclave, which was placed into a laboratory furnace where it was held at 170 °C for 20 h. The autoclave was then cooled in air. The resulting powders were separated by centrifugation for 5 min at 2000 rpm, washed with ethanol and deionized water several times, and dried overnight at 80 °C (yield: 92%). Finally, the dried solid was calcined in air at 425 °C for 4 h.

Characterization. Powder Diffraction. Powder X-ray diffraction measurements were carried out on a G670 diffractometer with an image plate detector (Huber, Rimsting, D) operating with Mo K α radiation ($\lambda = 0.07107$ nm).

IR Spectroscopy. Attenuated total reflection (ATR) spectroscopy was carried out on an Alpha ATR spectrometer equipped with a diamond crystal (Bruker, Karlsruhe, D). Solid samples were pressed on the crystal.

Scanning Electron Microscopy (SEM). Scanning electron microscopy measurements were performed with a high resolution SEM (Zeiss, LEO 1530 Gemini) with a thermally aided field emission gun (FEG) at an acceleration voltage of $U_{acc} = 0.2–30$ kV. For the SEM measurements, the CeO₂ nanopowders were placed on a carbon film, dried under vacuum for 20 min, and covered with gold to allow for a better electric conductivity.

Surface Area by N₂ Physisorption. Nitrogen physisorption experiments were carried out in a modified Autosorb 1C setup (Quantachrome). The sample was thermally pretreated at 200 °C in He for 2 h. The physisorption measurement was performed at the boiling point of liquid N₂ (78 K). The surface area was calculated according to the BET (Brunauer–Emmett–Teller) equation. The pore size distribution was obtained through the BJH (Barrett–Joyner–Halenda) method.

UV–Vis. UV–vis spectra were measured at room temperature on a Cary 5000 spectrometer (Varian, Palo Alto, U.S.A.) in reflection mode.

High-Resolution X-ray Photoelectron Spectroscopy (XPS). XPS measurements were carried out in an ultrahigh vacuum (UHV) setup equipped with a high-resolution Gammadata-Scienta SES 2002 analyzer. Monochromatized Al K α X-rays (1486.6 eV; anode operating at 14 kV and 55 mA) were used as incident radiation. The base pressure in the measurement chamber was around 2×10^{-10} mbar. XP spectra were recorded in the fixed transmission mode. The analyzer slit width was set to 0.3 mm, and pass energy of 200 eV was chosen, resulting in an overall energy resolution better than 0.5 eV. Charging effects were compensated by applying a flood gun. The binding energies were referenced to adventitious carbon (C 1s set to 284.8 eV). The CASA XPS program was employed to analyze the spectra. For determination of signal areas, a Shirley background was used. The O 1s signals were fitted with line shapes mixed from Gaussian and Lorentzian contributions.

Ultrahigh Vacuum Fourier Transform Infrared Spectroscopy (UHV-FTIRS). The UHV-FTIRS experiments on different ceria powder samples were performed in an UHV apparatus, which combines a state-of-the-art vacuum IR spectrometer (Bruker, VERTEX 80v) with a novel UHV system (PREVAC) (for details, see refs 27, 28). The base pressure in the measurement chamber was 2×10^{-10} mbar. The optical path inside the IR spectrometer and the space between the spectrometer and UHV chamber were evacuated to avoid adsorption of atmospheric moisture, resulting in superior sensitivity and stability

of the system. The polycrystalline ceria powders were first pressed onto a gold-plated stainless steel grid (0.5 cm × 0.5 cm) and then mounted on a sample holder, making it possible to record FTIR data in transmission geometry.

The grid and the attached powder particles were cleaned in the UHV chamber by heating to 750 K in order to remove all contaminations, such as water and hydroxyl groups. Prior to each exposure to CO, a spectrum of the clean powder was recorded as a background reference. We carried out the exposure of the sample to CO by backfilling the measurement chamber through a leak valve. The gas purity was 99.998 vol % for CO. All UHV-FTIR spectra were collected with 1024 scans at a resolution of 2 cm⁻¹ in transmission mode.

CO Oxidation. The oxidation of CO was studied at atmospheric pressure at temperatures in the range of 25–500 °C in a microcatalytic flow reactor (glass-lined U-tube, inner diameter 4 mm). The reactor was placed into a stainless steel block oven with hot rod heating elements controlled by a Eurotherm temperature controller. The temperature was ramped from 50 up to 500 °C with 5 K/min heating rate during the measurement. A mixture of 1% CO and 5000 ppm of O₂ in He was passed over 100 mg of CeO₂ with a flow rate of 100 mL/min. Both temperature and gas flows are controlled by software Lab View. Analysis of CO and CO₂ concentrations in the exhaust were performed using an Uras 26 infrared gas analyzer module (ABB Corp.).

RESULTS AND DISCUSSIONS

To evaluate the benefit of the sonochemical synthesis (sample identifier: S1), it was compared with microwave synthesis (sample identifier: S2), which is another nonconventional synthesis method allowing for quick heating rates, and classical ionothermal synthesis (sample identifier: S3). In a typical synthesis, the desired amount of cerium(III) acetate monohydrate was reacted with the necessary amount of NaOH in the ionic liquid under the conditions of the respective conversion method (see Experimental Section for details). To determine the phase purity and crystallinity of the obtained material, the XRD patterns for all samples were measured. As shown in Figure 1a, the sonochemical method results in pure CeO₂; all recorded diffraction peaks can be attributed to CeO₂ crystallizing in the CaF₂ structure type (PDF 34-394). No other crystalline phases are observable. The XRD patterns of

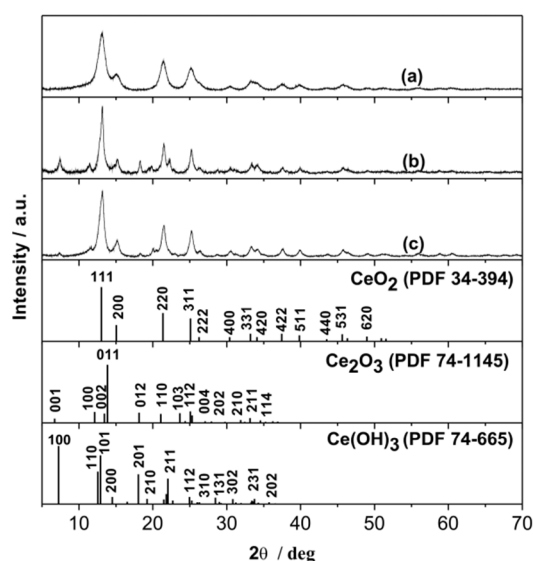


Figure 1. XRD patterns of as-prepared samples in [C₄mim][Tf₂N] synthesized by the ultrasound (a), microwave (b), and ionothermal routes (c), S1 through S3, respectively.

the materials obtained by microwave reaction (Figure 1b) and ionothermal synthesis (Figure 1c) show in addition peaks characteristic for Ce₂O₃ and Ce(OH)₃, albeit in different intensities. It is possible to convert the latter two samples to pure CeO₂ by calcination at 425 °C in air for 4 h (Figure S1, Supporting Information, shows the XRD patterns of the samples after calcination). The average crystallite sizes have been estimated applying the Scherrer equation to the most intense diffraction peak of CeO₂ which corresponds to *d*₍₁₁₁₎. This yielded crystallite sizes of approximately 4, 6.5, and 8.8 nm for samples prepared using the ultrasound (S1), microwave (S2), and ionothermal methods (S3), respectively. The data are summarized in Table 1, where the labels used for these

Table 1. Estimated Crystal Sizes, Lattice Parameters, and Cell Volumes of CeO₂ Samples Prepared in [C₄mim][Tf₂N] Using Different Preparation Methods

sample	grain size (nm)	lattice parameter (Å)	cell volume (Å ³)
S1 (sonochemical, as-obtained)	4.0	5.409(6)	158.2(3)
S2 (microwave, calcined at 425 °C)	6.5	5.381(5)	155.8(3)
S3 (ionothermal, calcined at 425 °C)	8.8	5.363(8)	154.2(4)

materials (in the states after post-treatment if applied) are introduced as well. There is a shift in the (111) diffraction peak position, with the material from the ionothermal route exhibiting the highest, and the material from sonochemical synthesis exhibiting the lowest angle, which is associated with an increase in the lattice constant as shown in Table 1 (Supporting Information). Moreover, from Table 1, we find that the lattice parameters of the prepared CeO₂ increase with decreasing crystallite sizes, a frequently observed phenomenon for oxide nanoparticles, which is due to increased lattice strain.^{29,30} For CeO₂, the presence of Ce³⁺ and/or oxygen vacancies also could lead to a lattice expansion.³¹

The morphology of the samples was investigated using SEM. It is shown in Figure 2 (left) that S1 is composed of aggregated spherical particles with a size of about 20 nm. When microwave

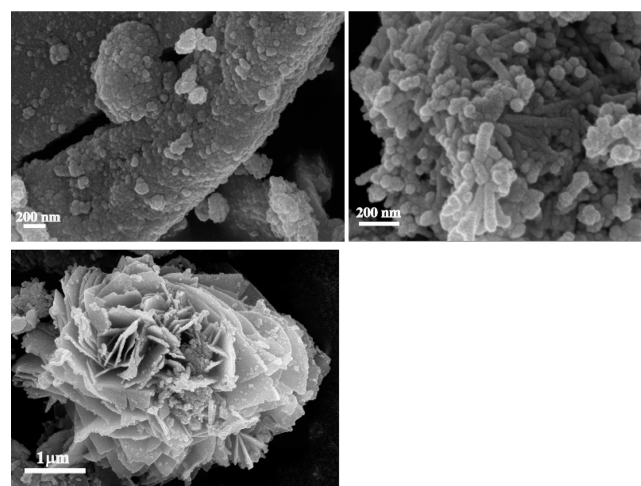


Figure 2. SEM images of CeO₂ prepared in [C₄mim][Tf₂N] using ultrasound (S1-as-prepared, left), microwave (S2-calcined, right), and the ionothermal route (S3-calcined, bottom).

irradiation was used, CeO₂ nanorods (S2-calcined, Figure 2, right) were obtained with widths of about 50 nm and lengths of about 300 nm. The ionothermal synthesis method leads to flower-like shaped nanostructures of CeO₂ (S3-calcined, Figure 2, bottom).

Structure and purity of the S1, S2, and S3 CeO₂ materials were also analyzed by Raman spectroscopy (Figure 3).

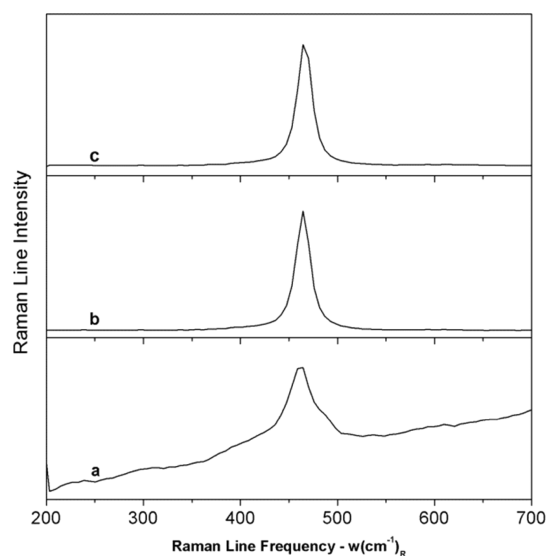


Figure 3. Raman spectra of CeO₂ prepared in [C₄mim][Tf₂N] by using (a) ultrasound (S1), (b) microwave (S2, calcined at 450 °C), and (c) the ionothermal synthesis route (S3, calcined at 450 °C).

Characteristic for fluorite-type CeO₂ is a band at about 464 cm⁻¹,³² which arises from the symmetrical stretching (F_{2g}) mode of the {CeO₈} unit.³³ As shown in Figure 3, a strong and broad band can be found at about 461 cm⁻¹ for S1 and at about 464 cm⁻¹ for S2 and S3, which can be assigned to the F_{2g} mode. This mode appears at lower frequencies for S1 than for S2 and S3. The values for S2 and S3 are similar to that reported for bulk CeO₂ in the literature (464 cm⁻¹).³² The red-shift for S1 is in agreement with the observation of a larger lattice constant. A broadening of the line can be an effect of defects in the oxygen sublattice resulting from thermal or grain size-provoked nonstoichiometry,³⁴ phonon confinement, and variations in phonon relaxation as a function of particle size strain.³⁵ The existence of a weak and less prominent broad band in sample S1 at about 600 cm⁻¹ can be assigned to a nondegenerate longitudinal optical (LO) mode of ceria. This occurs by the relaxation of symmetry rules, which in turn is associated with oxygen vacancies in the lattice. Furthermore, the presence of one more weak and broad band at 300 cm⁻¹ in S1 can be attributed to dislocation of oxygen atoms from their ideal fluorite lattice positions.³⁶

It is also possible to estimate the particle size from the Raman line broadening by using the following equation

$$\Gamma(\text{cm}^{-1}) = 10 + 124.7/D_R \quad (1)$$

where $\Gamma(\text{cm}^{-1})$ is the full width at half-maximum of the Raman active mode band, and D_R is the particle size of CeO₂ sample. The particle size (D_R) of the CeO₂ aggregates is 5.6 nm (S1), 14.7 nm (S2), and 14.4 nm (S3), respectively. The trend for the particles sizes estimated by this method is similar to the one from PXRD.

IR spectroscopy also allows insight into the chemical composition and the purity of the samples. Figure 4a–c

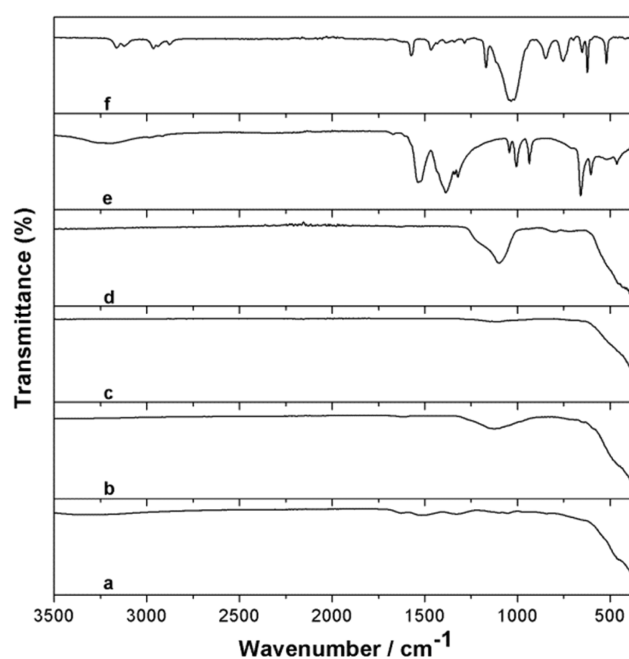


Figure 4. IR spectra of CeO₂ as-prepared in [C₄mim][Tf₂N] using (a) ultrasound (S1-as-prepared), (b) microwave (S2-calcined), (c) the ionothermal synthesis route (S3-calcined), (d) M-CeO₂, (e) cerium(III)acetate monohydrate, and (f) [C₄mim][Tf₂N].

shows the IR spectra recorded of samples S1–S3. Overall, the spectra are quite similar to the one of M-CeO₂ (Figure 4d). For all samples, an absorption band at about 455 cm⁻¹ can be observed, which originates from Ce–O stretching vibrations. The absorption bands at about 1125 and 1326 cm⁻¹ correspond to the characteristic vibrations of the Ce–O–Ce moiety. Moreover, the existence of absorbed water molecules on the surface of S1 is evident from the bands at 3324.7 and 1628 cm⁻¹, which are due to $\nu(\text{O–H})$ and $\delta(\text{O–H})$ vibrations. Comparing the IR spectra of S1–S3 with the IR spectra of [C₄mim][Tf₂N] and cerium(III) acetate monohydrate shows that these compounds are no longer present in the samples prepared using different preparation methods. They contain no starting materials, and the ionic liquid is removed completely by the cleaning step.^{37,38} The IR data of the sonochemically prepared sample are confirmed by TG analysis as shown in Figure S3 of the Supporting Information.

To check the constituents of the CeO₂ prepared by different preparation methods, EDX analysis was carried out during the SEM measurement (Figure S4, Supporting Information). As shown in Figure S4 of the Supporting Information, the EDX spectra show peaks corresponding to cerium and oxygen. The presence of carbon peak comes from the carbon film of the sample holder. No signals corresponding to elements from the ionic liquid from which the samples were obtained could be observed. This confirms the sample purity.

To get more detailed information about the oxidation states as well as the surface composition of the samples prepared via different synthesis methods, XPS measurements were carried out. Figure 5 shows the Ce 3d spectra obtained for the three as-prepared CeO₂ samples. The spin–orbit doublet with unprimed labels, v and u, corresponds to the primary Ce

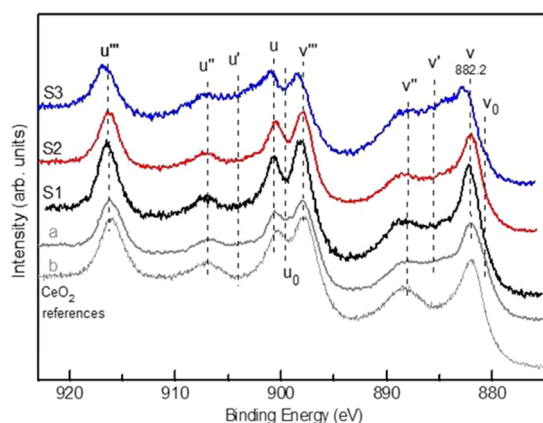


Figure 5. Ce 3d XPS spectra of as-prepared CeO₂ samples S₁, S₂, and S₃ compared with the reference CeO₂ samples: (a) M-CeO₂ and (b) from ref 40. The binding energies were calibrated to the C 1s peak at 284.8 eV.

3d_{5/2} and Ce 3d_{3/2} states, while the bands labeled v₀, v', v'', v''' and u₀, u', u'', u''' represent satellite features arising from the Ce 3d_{5/2} and Ce 3d_{3/2} ionization, respectively.³⁹ Furthermore, the dominating peaks at v, v'', v''' and u, u', u''' are characteristic for the Ce⁴⁺ species. Ce³⁺ is indicated by intensity at positions labeled v₀, v', and u₀, u'. By comparison with a spectrum of a well-crystalline CeO₂ from ref 40, it becomes obvious that the surface region all other CeO₂ materials including M-CeO₂ contain significant amounts of Ce³⁺, in particular the material obtained by the ionothermal route (S₃).

The exact analysis of the Ce³⁺ content from such spectra is, in principle, possible by fitting the signal shape with the corresponding component lines, but it is highly prone to errors. We used instead a simplified method, which takes advantage of the fact that intensity in the binding energy region of u''' arises from Ce⁴⁺ alone.³⁴ The method assumes that the surface of well-crystalline CeO₂ exposes exclusively Ce⁴⁺ (reduction degree: 0%, 100% Ce⁴⁺). This is not necessarily correct (cf. ref 40), but the method will relate the Ce⁴⁺ content in the surface regions of experimental samples to that of a reference, here taken from ref 40. From the spectra in Figure 5, the Ce⁴⁺ contents in the near-surface region of samples made via routes S₁, S₂, and S₃ and of M-CeO₂ were estimated to be 86%, 93%, 67%, and 86%, respectively, of that in well-crystalline CeO₂.⁴¹

The corresponding O 1s spectra are dominated by a major signal centered at 529.6 eV (Figure S5, Supporting Information), which originates from the bonding of oxygen anions to cerium centers.^{42,43} A second O 1s peak at about 532.2 eV is ascribed primarily to the existence of hydroxyl species formed at surfaces of the as-prepared CeO₂ samples.

The surface area exposed by the different samples was elucidated by nitrogen adsorption–desorption isotherm measurements. Figure 6 reveals some differences in the shape of the N₂ adsorption–desorption isotherms of the samples. The shape of the hysteresis loops of the samples corresponds to a type IV isotherm according to the IUPAC classification, indicating a mesoporous structure of the samples. For S₁, the hysteresis loop is a composite of the H2 and H3 types, indicating that the sample has channel-like or ink-bottle pores. The hysteresis loops for S₂ and S₃ are a composite of H1 and H3, suggesting they may have slit-shape pores or plate-like particles. The values of the BET surface area calculated from

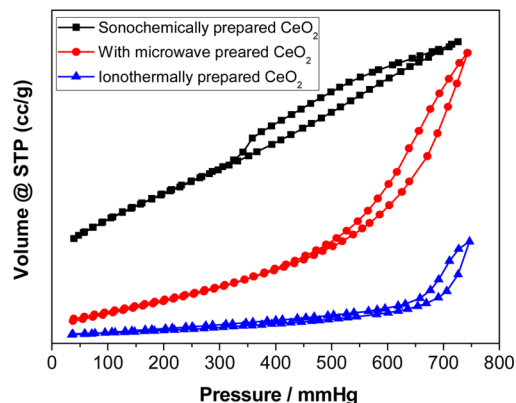


Figure 6. N₂ adsorption–desorption isotherm of as-prepared CeO₂ using different preparation methods.

the linear part of the nitrogen adsorption isotherm plot at 77 K are 162 m²/g for the sonochemically prepared CeO₂ nanoparticles (S₁), 81 m²/g for CeO₂ nanorods obtained via microwave synthesis (S₂), and 22 m²/g for ionothermally synthesized CeO₂ flower-like particles (S₃). All values are considerably higher compared to the reported value for M-CeO₂ (3.1 m²/g).⁴⁴ The most frequent pore diameter derived from the nitrogen adsorption isotherm by the BJH method (Figure S6, Supporting Information) was 1.83 nm for sonochemically prepared CeO₂ (S₁), with a narrow pore size distribution, while the pore size distributions were broad around 4 and 8 nm for the samples prepared via the microwave (S₂) and ionothermal (S₃) routes, respectively. The BET measurement can also be used to approximate the particle diameter. For spherical particles, the specific surface area (SSA) of a particle can be calculated according to

$$SA = 6/\rho D \quad (2)$$

here ρ is the density of the material, and D is the particle diameter. The density of bulk ceria is 7 g/cm³. However, because the particles obtained via the ionothermal (S₃) and microwave (S₂) routes are not spherical, eq 2 can only be used for the sonochemically prepared nanospherical CeO₂. The result is 5.2 nm, which matches well with the particle size determined from PXRD and eq 1.

Optical Properties of CeO₂. The optical properties of the samples were determined by recording the absorption spectra in the range of 325–700 nm (Figure 7, top). An absorption edge at about 345 nm could be evidenced for the CeO₂ nanorods and flower-like morphologies (routes S₂ and S₃) and at about 360 nm for the sonochemically prepared CeO₂ nanoparticles (S₁). The charge–transfer transition between the O²⁻ (2p) and Ce⁴⁺ (4f) bands is responsible for this UV absorption.⁴⁵ The optical band gap (E_g) can be calculated on the basis of the optical absorption spectrum by the following equation

$$(Ah\nu)^n = B(h\nu - E_g) \quad (3)$$

where h is Planck's constant, ν is the frequency of light, A is the absorbance, B is a materials constant, and n is either 2 for an indirect allowed transition or 1/2 for a direct allowed transition. Figure S7 of the Supporting Information shows the $(Ah\nu)^2$ versus $h\nu$ curve for the sample for the direct transitions. The band gaps of the CeO₂ nanoparticles (S₁), nanorods (S₂), and nanoflowers (S₃) are determined to be about 2.56, 2.45, and

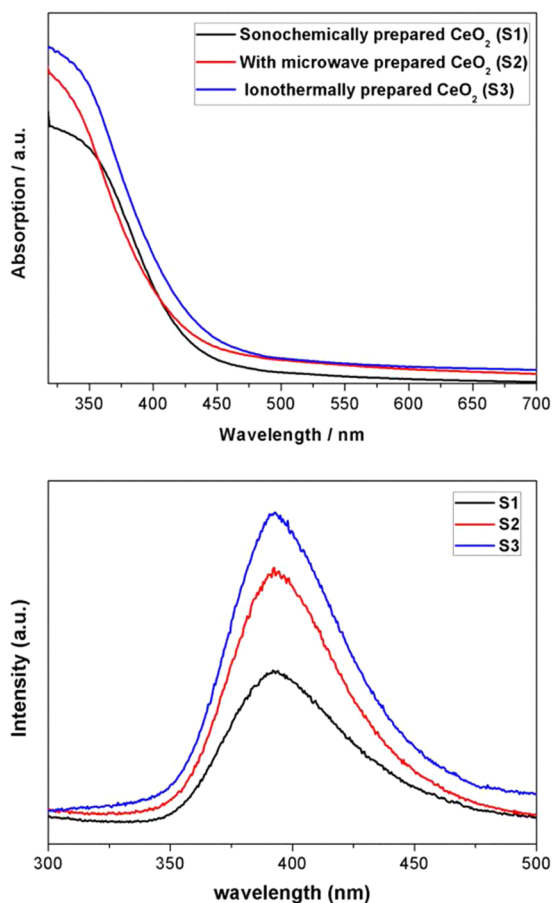


Figure 7. UV-vis absorption (top) and room temperature photoluminescence (bottom) spectra of CeO₂ nanoparticles (S1-as prepared), nanorods (S2-calcined), and flower-like (S3-calcined).

2.41 eV, respectively, estimated from the intersection of the extrapolated linear portions with the abscissa. It is well known that the red shift for the band gap in the CeO₂ samples compared to that of bulk CeO₂ (3.15 eV)⁴⁶ can arise from defects in the fluorite structure of CeO₂, namely, due to the existence of Ce³⁺ and related O²⁻ vacancies. This initiates intermediate energy levels causing a decrease in the band gap.

From these band gaps, E , the average crystallite sizes can be estimated by eq 4⁴⁷

$$E = E_0 + \frac{h^2}{8\mu R^2} \quad (4)$$

where E_0 is the energy gap for bulk materials, and h is Planck's constant. R denotes the particle radius of the studied material, and μ is the reduced mass of exciton, which can be calculated from

$$\frac{1}{\mu} = \frac{1}{m_e} + \frac{1}{m_h} \quad (5)$$

m_e and m_h are the electron and hole effective masses, respectively. From our data, the particle sizes are approximately 5.6, 5.1, and 5 nm for CeO₂ prepared using the ultrasound (S1), ionothermal (S2), microwave methods (S3), respectively. In contrast to the grain size obtained from the BET surface area (eq 2) for S1, which is in good agreement with the value obtained using the Scherrer formula and eq 1, the values for S2

and S3 are less than that determined using Scherrer formula and eq 1.

The room temperature photoluminescence (PL) spectra of the as-obtained CeO₂ nanoparticles (S1) and CeO₂ nanorods (S2) from the microwave route and ionothermally prepared flower-like CeO₂ (S3) were recorded (Figure 7, bottom) using a 295 nm filter with an excitation wavelength of 250 nm. Strong UV emissions at ~393 nm was observed in the nanoparticles (S1), nanorods (S2), and flower-like particles (S3), which comes from defects including oxygen vacancies in the crystal with electronic energy levels below the 4f band. These defects act as radiative recombination centers for electrons initially excited from the valence band to the 4f band of the oxide.^{48,49}

CO Adsorption Studies. The structural and electronic properties of all as-prepared CeO₂ samples using the ultrasound (S1-as-prepared), microwave (S2-calcined), and ionothermal routes (S3-calcined) were further probed by CO adsorption using vibrational spectroscopy. For comparison, the adsorption of CO on the commercial M-CeO₂ was first investigated. Figure S8 of the Supporting Information displays the UHV-FTIR spectra recorded after exposing the clean M-CeO₂ sample to CO at 90 K and subsequently heating to the indicated temperatures. After CO adsorption at 90 K, two C–O stretching bands are resolved at 2174 and 2160 cm⁻¹, which originate from CO molecules adsorbed at coordinatively unsaturated (CUS) surface Ce⁴⁺ and Ce³⁺ sites, respectively.⁵⁰ The existence of two Ce cation species is further confirmed by the temperature-dependent IR data (Figure S8b, Supporting Information). Upon heating under vacuum, the CO band at 2160 cm⁻¹ shows a rapid decrease in intensity and vanishes completely around 130 K, while the intense IR band at 2174 cm⁻¹ diminishes gently and shifts slightly to higher frequency at 2179 cm⁻¹ before it disappears at 160 K.

The corresponding binding energies are estimated to amount to about 42 kJ/mol for CO on Ce⁴⁺ and 34 kJ/mol for CO on Ce³⁺, revealing that CO is more strongly bound to Ce⁴⁺ sites. The enhanced interaction between CO and Ce⁴⁺ can be explained by the higher Lewis acidity of Ce⁴⁺ than Ce³⁺ cations. As a consequence, one would expect the 5σ donation from CO to Ce⁴⁺ to be increased, thus causing enhancement of the CO binding energy and a blue shift of the C–O stretch band, as observed for CO adsorption on CO₂-pretreated ZnO surfaces.^{51,52}

As shown in Figure 8a, CO adsorption on the sonochemically prepared CeO₂ sample (S1) at 90 K leads to the appearance of one dominating IR band at 2165 cm⁻¹ with a shoulder centered at 2174 cm⁻¹. Upon heating to 120 K (Figure 8b), the 2165 cm⁻¹ band shrinks substantially, while the band at 2174 cm⁻¹ remains stable in intensity and shifts to 2185 cm⁻¹. Its complete desorption takes place at about 160 K. On the basis of the frequency and thermal stability data, the bands at 2165 and 2174 cm⁻¹ are assigned to CO molecules bound to surface Ce³⁺ and Ce⁴⁺ CUS sites, respectively. The shift of the Ce⁴⁺-related CO band from 2174 to 2185 cm⁻¹ could be attributed to the slight modification of the electron density at the Ce cations induced by the decrease of CO coverage.

Figure 9 shows the IR data obtained after CO adsorption on the ionothermally prepared CeO₂ sample (S3) at 90 K and then heating to different temperatures. Only one C–O stretch band is observed at 2177 cm⁻¹, which shifts to 2185 cm⁻¹ at higher temperatures and disappears nearly completely at about 160 K. This band is characteristic for the CO species adsorbed on

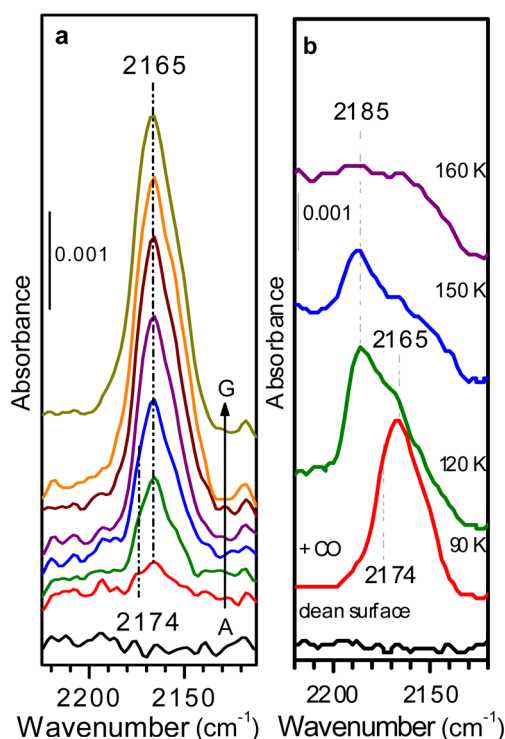


Figure 8. UHV-FTIR spectra obtained after (a) exposing clean sonochemically prepared CeO₂ nanoparticles (S1) to different doses of CO at 90 K in a UHV chamber: (A) clean surface, (B) 5×10^{-7} mbar, (C) 1×10^{-6} mbar, (D) 5×10^{-6} mbar, (E) 1×10^{-5} mbar, (F) 5×10^{-5} mbar, and (G) 1×10^{-4} mbar CO and then (b) heating to the indicated temperatures. Prior to CO adsorption, S1 was cleaned by heating to 800 K in UHV and then cooled to 90 K.

surface Ce⁴⁺ CUS sites, in accordance with the results for the M-CeO₂ and S1 samples. However, the IR spectra for the S3 sample do not show any peaks originating from CO bound to Ce³⁺ sites.

In summary, the present IR spectra demonstrate the coexistence of Ce⁴⁺ and Ce³⁺ cations on the surface of the S1 sample where Ce³⁺-related CO was detected as major species. For the S3 sample, only the surface Ce⁴⁺ site was identified by CO adsorption experiments. However, the XPS data (Figure 5) confirm the presence of both Ce⁴⁺ and Ce³⁺ cations, with the former being predominant for all the three as-prepared CeO₂ samples. This discrepancy between the IR and XPS results can be explained by the fact that the IR data of CO adsorption provide only information on Ce cation sites at the top surface layer. However, in XPS, chemical information from a depth of several nanometers is averaged. The IR data (Figure 8) reveal that for the sonochemically prepared CeO₂ sample (S1) the surface concentration of Ce³⁺ is very significant and clearly higher than in the ionothermally prepared sample (S₃). The reduction of Ce⁴⁺ to Ce³⁺ is accompanied by the formation of surface oxygen vacancy sites, which have been considered to play a crucial role in the catalytic activity of oxides. Indeed, the catalysis experiments (see below) prove that the S1 sample exhibits the highest activity for CO oxidation, whereas the catalytic activity of the ionothermally prepared CeO₂ sample (S3) is much lower. This corresponds to the fact that no surface Ce³⁺ species were identified for the S3 sample.

In addition, it should be noted that the electronic structure of the metal sites could be modified with different synthesis methods, thus resulting in a change in the Lewis acidity of

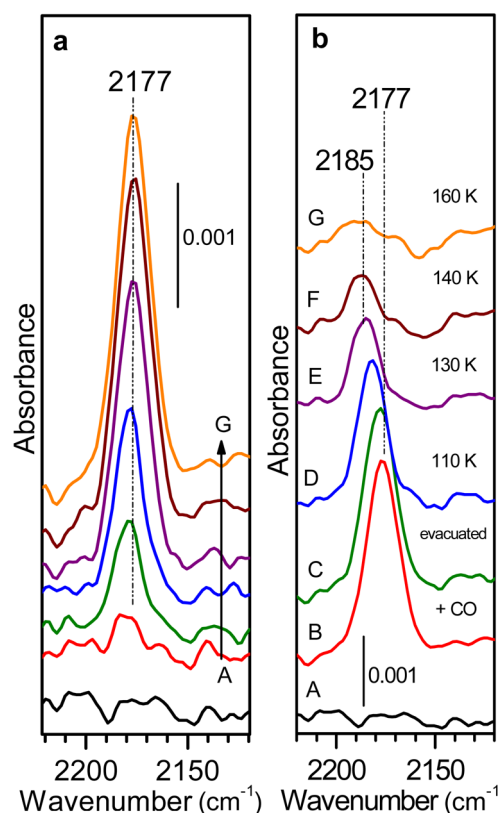


Figure 9. UHV-FTIR spectra obtained after (a) exposing clean with ionothermally prepared CeO₂ nanoparticles (S3) to different doses of CO at 90 K in a UHV chamber: (A) clean surface, (B) 5×10^{-7} mbar, (C) 1×10^{-6} mbar, (D) 5×10^{-6} mbar, (E) 1×10^{-5} mbar, (F) 5×10^{-5} mbar, and (G) 1×10^{-4} mbar CO and then (b) heating to the indicated temperatures. Prior to CO adsorption, S3 was cleaned by heating to 800 K in UHV and then cooled to 90 K.

surface Ce cations. One would expect that a lower Lewis acidity of a Ce cation decreases the binding strength of CO with this site. The lack of the Ce³⁺-related CO band for the S3 sample (Figure 9) may also be related to a less stable Ce³⁺-CO binding that cannot be detected at 90 K.

The catalytic activities of CeO₂ obtained by different methods were evaluated in CO oxidation as shown in Figure 10, and significantly different activities were observed. The CO oxidation begins at a temperature of 175 °C in the case of sonochemically prepared CeO₂ (S1), and the conversion rapidly increased to 100%. In the case of ionothermally (S3)

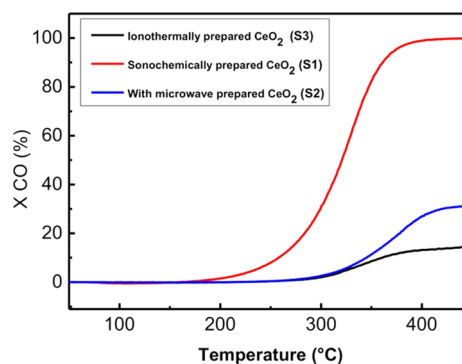


Figure 10. CO oxidation over CeO₂ obtained by different preparation methods.

and microwave-prepared CeO₂ (S2), the reaction starts at 285 °C. Sonochemically prepared CeO₂ showed better performance than those prepared ionothermally or with microwaves. Conversions obtained at 400 °C were 100%, 30%, and 14%, respectively.

The ranking of the catalytic activity corresponds to the ranking in surface area. The surface area of the sonochemically prepared CeO₂ nanoparticles (S1) is 162 m² g⁻¹ but that of the CeO₂ nanorods (S2) is 81 m² g⁻¹, and the ionothermally prepared flower-like CeO₂ (S3) exhibits only 22.2 m² g⁻¹. A large surface to volume ratio of the CeO₂ nanoparticles in comparison to the nanorods (S2) and flower-like nanostructures (S3) can provide a larger number of active sites and consequently higher conversions of for CO. However, the differences in activity are clearly more pronounced than the variation of the surface area. Therefore, the presence of structural defects and oxygen vacancy should also have an influence on the activity. Oxygen vacancies can act as promoting sites for CO conversion, as supported by the UHV-FTIRS results discussed above.

Effect of the Cerium Source. Morphology and crystallization of CeO₂ can be influenced also by other reaction parameters than the transformation method. To investigate the influence of the cerium source, other cerium precursors including cerium(III) nitrate hydrate and cerium(III) trichloride hydrate were used instead of cerium(III) acetate hydrate, while the other reaction conditions for the sonochemical synthesis are the same. The SEM image of as-prepared CeO₂ from cerium(III) nitrate hydrate as the precursor shows the formation of CeO₂ nanoparticles with average diameter of about 5 nm (Figure 11). When cerium(III)

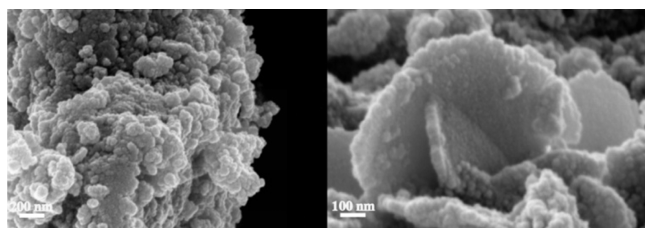


Figure 11. SEM images of sonochemically prepared CeO₂ nanoparticles from cerium(III) nitrate hydrate (left) and CeO₂ nanosheets prepared from cerium(III) chloride hydrate (right).

chloride hydrate was used as a precursor, CeO₂ nanosheets were obtained. These results are in accordance with previous results reported by Elidrissi et al.,⁵³ who observed the formation of CeO₂ nanosheets from an aqueous solution of cerium(III) chloride hydrate. In all cases, phase pure CeO₂ was obtained, but the morphology of the product varied from nanospheres to nanosheets. This shows that the cerium precursor plays a key role in determining the cerium morphology. The effect of different precursors on the morphology of the final product can be due to different reaction kinetics, namely, the hydrolysis rate, but also the ionic strength of the solvent can affect the nucleation process. Furthermore, after ionolysis, the counterions can act as ligands and can influence the morphology by preferential coordination to the growth facets.^{54,11}

Sonication Time and Drying Temperature. To check the influence of irradiation time on the particle morphology, a series of experiments were carried out with reaction times varying between 1 and 12 h. A total of 0.2 g of cerium(III) acetate monohydrate was used together with 0.1 g of sodium

hydroxide in 2 mL of [C₄mim][Tf₂N]. The XRD patterns (Figure S9, Supporting Information) indicate that the crystallinity and particle size of the as-prepared CeO₂ are dependent on the irradiation time, where the as-obtained samples were characterized by XRD. As shown in Figure S9 (top) of the Supporting Information, the diffraction peaks of as-prepared CeO₂ at 9 h are much sharper than those of as-prepared CeO₂ at 1 h. It is found that the particle size of CeO₂ increases with increasing the irradiation time from 1 to 12 h, which is 4 nm at 9 h, but further increasing of the irradiation time beyond 9 h does not alter the particle size any more. Figure S11 of the Supporting Information shows XRD patterns of the sonochemically prepared CeO₂ after drying at different drying temperatures from 30 to 90 °C. The patterns in Figure S11 of the Supporting Information show that the increase in the drying temperature causes no remarkable change in the crystallinity. These results verify that the sonication process yield nanocrystalline CeO₂ directly without going noticeably through an intermediate phase such as hydroxides, thus there is no need for sample calcination.

Effect of Precipitator. To evaluate the effect of the precipitator on the morphology, crystallinity, and particle size, NaOH (pK_b = -0.8) was replaced with an aqueous solution of NH₄OH (pK_b = 4.75) (equal molar ratio) under otherwise identical conditions. Although PXRD shows that the sample consists of fluorite-type ceria (Figure S12, Supporting Information), the crystallinity is noticeably less compared to the samples that are prepared with NaOH. As shown in Figure 12, the as-prepared sample is composed of nanospherical CeO₂

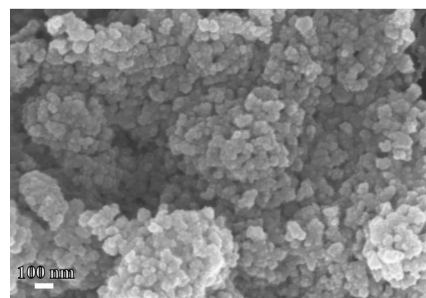
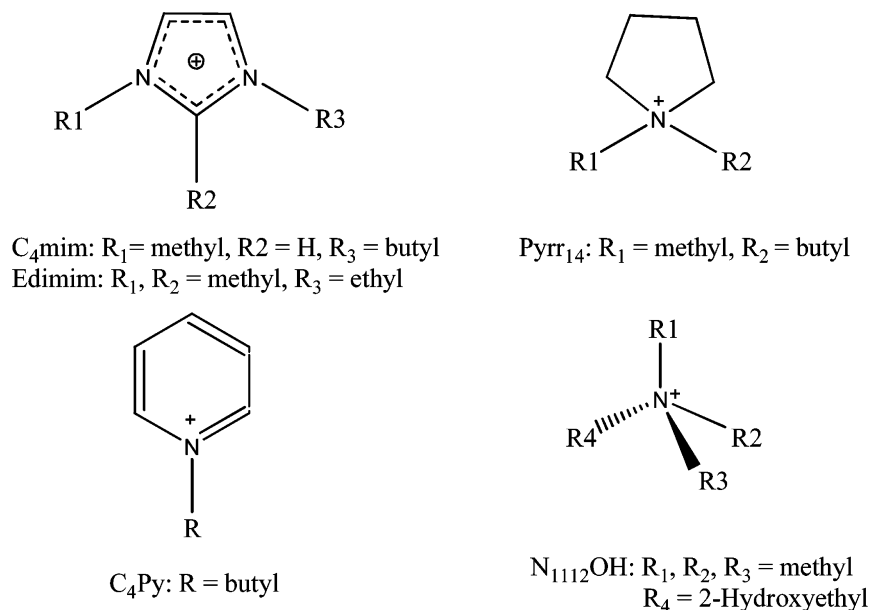


Figure 12. SEM image of CeO₂ prepared via sonochemical synthesis with NH₄OH as the precipitator.

with a particle size in the range 50–100 nm. Figure S13 of the Supporting Information shows the nitrogen-adsorption-desorption isotherm of CeO₂ prepared using NH₄OH; the BET surface area of CeO₂ obtained using NH₄OH (133 m² g⁻¹) is significantly less than that of CeO₂ prepared using NaOH (162 m² g⁻¹). These observations are in agreement with previous reports about the effect of the precipitator on the crystallinity and morphology of nanometal oxides. It was demonstrated that the precipitator has a remarkable influence on the morphology of ZnO nanocrystals, where substituting NaOH with NH₄OH led to formation of ZnO nanoparticles with an average size less than 10 nm instead of belt-like ZnO nanowires.⁵⁵ Mai found that the mesoporous CeO₂ prepared using NaOH by the precipitation method with cetyltrimethylammonium bromide as the templating agent at 400 °C shows larger surface area (205 m² g⁻¹) than that of the mesoporous CeO₂ prepared using NH₄OH (166 m² g⁻¹) and that in the case of Na₂CO₃ no mesoporous structures could be detected.⁵⁶

Scheme 1. IL Cations Used in This Study



Variation of the Ionic Liquid. There are studies that provide evidence that ILs can act as templates and influence the structure and surface properties of nanoparticles. The formation of small particles can be attributed to the higher nucleation rates of nanomaterials in ionic liquids. To check the influence of the structure of ionic liquids on the morphologies and the crystallization of sonochemically prepared CeO_2 , four different ionic liquids, all with the same anion, were tested (Scheme 1). The bis(trifluorosulfonyl)amide anion is weakly coordinating, and previous studies have shown that the anions in fact have little direct impact on particle formation and growth compared to the cation.^{57,58}

On the basis of the nature of the IL, the interaction energies can be variable as well as the organization of IL.⁵⁹ Furthermore, depending on the fact that the CeO_2 crystals are polarly composed of positively charged Ce layers and negatively charged O layers and the different cationic structures of the ionic liquid, different mechanisms including electrostatic attraction, hydrogen bonds, π - π stacking interaction, and self-assembly mechanism can be expected to occur between ionic liquids and the unit growth of CeO_2 , leading to control of the growth rate in a certain direction.⁶⁰

The cations were chosen for the following reasons. Imidazolium-based ionic liquids are among the most commonly used species because of their unusual physical and chemical properties. The $[C_4mim]^+$ cation contains an aromatic core, which can participate in π -interactions. It offers a highly electron accepting region and is likely to be responsible for the electrostatic attraction with polar moieties on the surface of particles.⁶⁰ An acidic proton is attached to the aromatic ring structure, which could act as a bridging species through hydrogen bonding. It is believed that both electrostatic and coordination effects of imidazolium cations contribute to nanoparticle stabilization in the ionic liquid.⁶¹ The presence of the alkyl chain is thought to control the size distribution and agglomeration of the nanoparticles in dispersion.⁶² $[Edimim]$ also contains an imidazolium core like $[C_4mim]^+$, but it does not possess any acidic protons. $[C_4Py]^+$ is a pyridinium-based cation. It does not possess any acidic protons like the

imidazolium-based cations, but the aromatic group is still present. The pyrrolidinium $[Pyrr_{14}]$ cation is a quaternary ammonium, which does not possess either an acidic proton or aromatic ring system. $[N_{1112}OH]$ is a saturated quaternary ammonium cation with $-OH$ functionality in the side chain.

We found with this series that the structure of ionic liquids has an important influence on the morphology, crystallinity, and particle size of the products. Figure 13a shows the

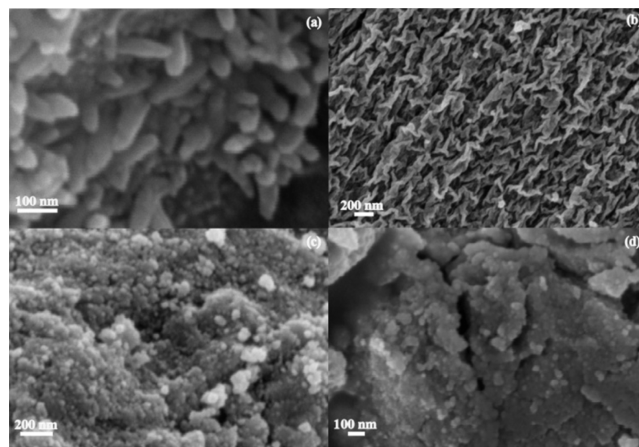


Figure 13. SEM images of as-obtained CeO_2 in (a) $[Edimim][Tf_2N]$, (b) $[Pyrr_{14}][Tf_2N]$, (c) $[C_4Py][Tf_2N]$, and (d) $[N_{1112}OH][Tf_2N]$.

morphology of the product derived from using $[Edimim][Tf_2N]$, which is composed of nanorods with 20 nm diameter and 100–150 nm length. When $[Pyrr_{14}][Tf_2N]$ is used, the as-prepared sample is composed of ribbon-like shaped particles (Figure 13b). Nanospherical CeO_2 with a crystal size of 10 nm formed when $[C_4Py][Tf_2N]$ and $[N_{1112}OH][Tf_2N]$ are used as shown in Figure 13c and d.

The PXRD data (Figure 14) confirm that in all ionic liquids phase pure CeO_2 could be directly obtained. No diffraction peaks of the starting material, cerium(III) acetate, or other cerium oxides and hydroxides can be evidenced. The crystal domain sizes (d_{hkl}) have been estimated from the most intense

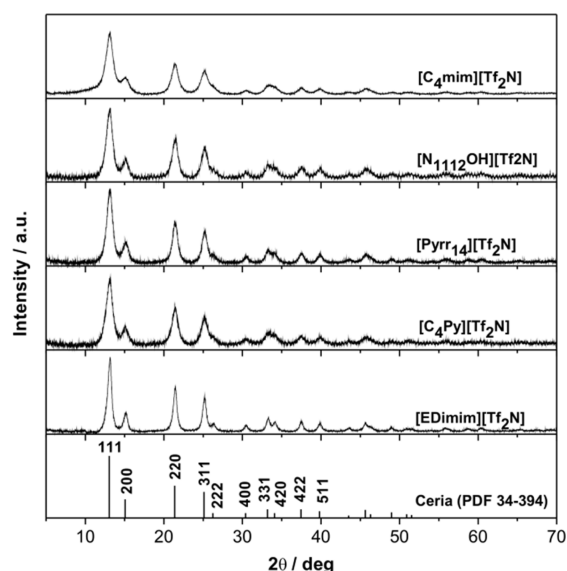


Figure 14. XRD patterns of CeO₂ prepared in different ionic liquids (uncalcined); database pattern of ceria given for comparison.

diffraction peak (111) using the Scherrer equation. The crystallite sizes vary from 3.2 to 5.7 nm (Table 2). The sample

Table 2. Estimated Grain Size of Crystallographic plane (111) and Texture Properties of CeO₂ Prepared in Ionic Liquids (Uncalcined)

sample	S_{BET} ($\text{m}^2 \text{g}^{-1}$)	grain size (nm)	surface area	pore volume, V_{pore} ($\text{cm}^3 \text{g}^{-1}$)	pore size (nm)
[C ₄ mim][Tf ₂ N]		4.0 ± 0.2	162	0.16	1.83
[N ₁₁₁₂ OH][Tf ₂ N]		3.9 ± 0.2	128	0.13	1.8
[Pyrr ₁₄][Tf ₂ N]		3.7 ± 0.2	91	0.06	1.8
[C ₄ Py][Tf ₂ N]		3.2 ± 0.2	95	0.09	1.8
[EDimim][Tf ₂ N]		5.7 ± 0.2	78	0.09	1.8

prepared in [EDimim][Tf₂N] showed better crystallinity and a larger crystal particle size of 5.7 nm, and the sample prepared in [C₄Py][Tf₂N] showed the smallest crystallite size of 3.2 nm.

The nitrogen adsorption–desorption isotherms and corresponding pore size distributions of the synthesized samples are shown in Figure 15 and Figure S14 of the Supporting Information, respectively; the texture properties are listed in

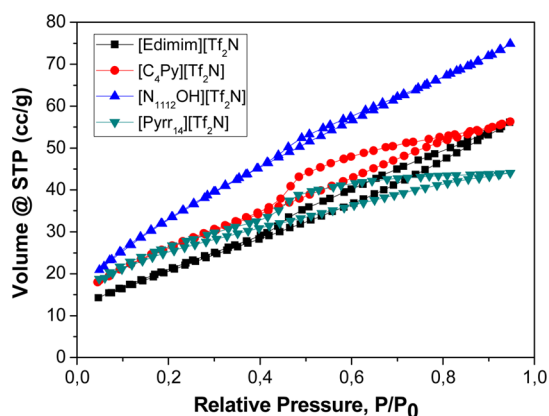


Figure 15. N₂ adsorption–desorption isotherms of the synthesized CeO₂ samples in different ionic liquids.

Table 2. The isotherms of the synthesized samples are of type IV with a hysteresis loop of the H2 type, characteristic of mesoporous materials, according to the IUPAC classification. The specific surface area values range from 78 $\text{m}^2 \text{g}^{-1}$ for the material prepared in [EDimim][Tf₂N] to 163 $\text{m}^2 \text{g}^{-1}$ for the sample prepared in [C₄mim][Tf₂N]. The pore size distribution for the as-prepared samples was determined by the BJH method from the adsorption branch. One rather narrow peak with a maximum at 1.8 nm was observed on a broad background extending to 6 nm (Figure S14, Supporting Information). The porosity arising from the interparticle space of the CeO₂ samples can be attributed to the organized agglomeration of monodisperse CeO₂ particles obtained by ionolysis under ultrasound irradiation.

The hysteresis loops for the nitrogen adsorption–desorption experiments on the CeO₂ samples prepared in [C₄mim][Tf₂N], [C₄Py][Tf₂N], and [Pyrr₁₄][Tf₂N] show a triangular shape and a steep desorption branch, which can be ascribed to the pore connectivity effect resulting from formation of pores with narrow mouths (ink-bottle pores).

Moreover, all samples show very high surface areas (Table 2), which are substantially larger than that reported for M-CeO₂ (3.1 $\text{m}^2 \text{g}^{-1}$) as well as those of previously reported for double-shelled CeO₂ synthesized by a solvothermal method using a solvent mix of PEG-400 (poly(ethylene glycol)) and H₂O (47 $\text{m}^2 \text{g}^{-1}$)⁶³ or mesoporous CeO₂ prepared via heating Ce(NO₃)₃ in 1-allyl-3-methylimidazolium chloride containing cellulose (62 $\text{m}^2 \text{g}^{-1}$).⁶⁴ However, the surface areas of the CeO₂ samples prepared in different types of ionic liquids are lower than those of spherical aggregates of CeO₂ particles prepared solvothermally using 1-hexadecyl-3-methylimidazolium bromide [C₁₆mim][Br] and ethanol (227 $\text{m}^2 \text{g}^{-1}$).⁶⁵

The CO conversions as a function of temperature by the as-prepared CeO₂ in different ionic liquids and of bulk ceria are shown in Figure 16. Obviously, the materials prepared in the

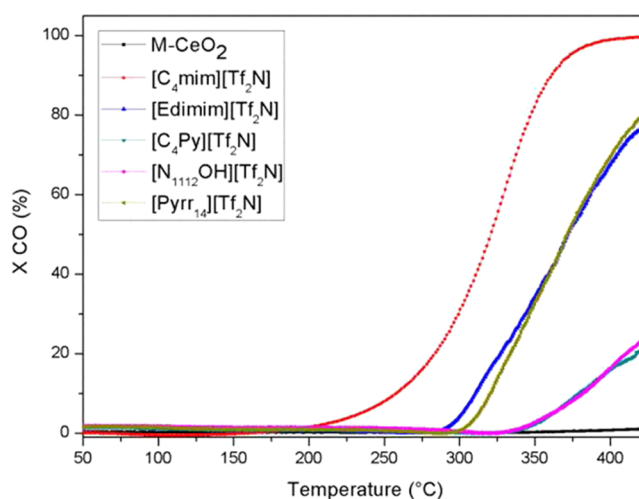


Figure 16. Catalytic activity for CO oxidation of CeO₂ prepared in different ionic liquids in comparison with bulk ceria (M-CeO₂).

other ILs cannot compete with the one made in [C₄mim][Tf₂N] with respect to CO oxidation activity. While the former achieved full conversion already below 400 °C, the CeO₂ made in [Pyrr₁₄][Tf₂N] achieved 70%, that prepared in [EDimim][Tf₂N] converted 70%, CeO₂ obtained in [N₁₁₁₂OH][Tf₂N] achieved 16%, and that prepared in [C₄Py][Tf₂N] converted

16%, all at 400 °C. It is also clear that M-CeO₂ (<5 μm) exhibits inferior activity compared with nanosized samples (<1.5%, 400 °C).

As mentioned above, the differences cannot be rationalized in terms of surface area, although the sample prepared in [C₄mim][Tf₂N] with the highest surface area (162 m² g⁻¹) exhibits the highest activity; CeO₂ prepared in [N₁₁₁₂OH]-[Tf₂N] has a surface area of the same order (128 m² g⁻¹) but is a much poorer catalyst. It is, however, well known that nanocrystalline metal oxide catalysts with high surface area exhibit a large number of active sites such as crystal facets, oxygen vacancies, edges, and corners for the adsorption of reactants that can result in better catalytic performance.⁶⁶ Indeed, apart from the surface area the high catalytic activity of CeO₂ can be explained by the oxygen vacancy formation and migration, where the oxygen vacancy formation provides freedom for the movement of lattice oxygen, thus increasing the mobility of oxygen on ceria and improving the catalytic performance.^{56,67} This is further supported by our UHV-FTIRS results (Figures 8 and 9) that provide direct spectroscopic evidence that the high catalytic activity of the CeO₂ samples is related to the high concentration of surface oxygen vacancy sites (whereby the Ce³⁺ ions are formed).

CONCLUSIONS

In summary, various nanostructured CeO₂ materials were successfully synthesized by one-step ultrasound synthesis with different kinds of ionic liquids directly without subsequent thermal treatment. This method is simple, one-step, and reproducible, and there is no need to use templates or surfactant because the ionic liquid acts as solvent and template. Control of the reaction conditions such as the heating method, chemical nature of the ionic liquid, Ce precursor, and nature of the precipitator allows preparation of CeO₂ with different morphologies. The heating method exerts a crucial impact on the final structure and morphologies of ceria, where nanorods and flower-like shapes were obtained in [C₄mim][Tf₂N] using microwave and ionothermal synthesis methods, whereas nanospheres were obtained using ultrasound. The dependence of the morphology of ceria on the structure of the ionic liquid was studied. Varying the cation of the ionic liquid resulted in a change in the morphology of ceria from nanospheres ([C₄mim]⁺, [C₄Py]⁺, and [N₁₁₁₂OH]⁺, average crystal sizes of 5–10 nm) to nanorods with 20 nm diameter and 100–150 nm length ([Edimim]⁺) and ribbon-like shapes ([Pyrr₁₄]⁺). Moreover, using different Ce sources (chloride or nitrate instead of acetate) resulted in the formation CeO₂ nanosheets. The precipitator also exhibited an important influence on the morphology, crystallinity, and particle size of the products. The samples prepared using different ionic liquids showed different catalytic activities for CO oxidation. The highest catalytic activity was obtained for the material prepared from cerium acetate via the sonochemical route with NaOH in [C₄mim]-[Tf₂N], which is related to the high concentration of surface oxygen vacancies created by the reduction of Ce⁴⁺ to Ce³⁺ cations as evidenced by the UHV-FTIRS data. This material exhibited full CO conversion under conditions where conventional CeO₂ achieved no conversion at all. This shows how tremendously important the selection of reaction parameters is and that it is important to study unconventional yet green preparation methods for catalysts.

ASSOCIATED CONTENT

Supporting Information

XRD patterns of calcined CeO₂ synthesized by using different preparation methods; XRD patterns (2θ = 12–14°) of calcined CeO₂ synthesized by ultrasound, microwave, and ionothermal process; TG curve of the sonochemically prepared CeO₂ powder in [C₄mim][Tf₂N]; EDX spectra of as-prepared CeO₂ (S1-as-prepared), (S2-calcined), and (S3-calcined); O 1s spectra of CeO₂ samples prepared using different preparation methods; UHV-FTIR spectra obtained after (a) exposing clean Aldrich CeO₂ (M-CeO₂); XRD patterns of CeO₂ prepared in [C₄mim][Tf₂N] via sonochemical synthesis using different reaction times; XRD patterns of CeO₂ prepared via sonochemical synthesis using different cerium source; XRD patterns of CeO₂ at different aging temperature; XRD patterns and N₂ adsorption–desorption isotherm of CeO₂ prepared via sonochemical synthesis with NH₄OH as precipitator instead NaOH in ionic liquid; and pore size distribution curves of the synthesized CeO₂ samples in different ionic liquids. This material is available free of charge via the Internet at <http://pubs.acs.org>.

AUTHOR INFORMATION

Corresponding Author

*E-mail: mudring@iastate.edu.

Notes

The authors declare no competing financial interest.

ACKNOWLEDGMENTS

We would like to thank Dr. Dennis Großmann for help with the catalytic studies. This work is supported in part by the DFG Cluster of Excellence RESOLV and the Critical Materials Institute, an Energy Innovation Hub funded by the U.S. Department of Energy, Office of Energy Efficiency and Renewable Energy, Advanced Manufacturing Office.

REFERENCES

- (1) Sun, C.; Li, H.; Chen, L. Nanostructured ceria-based materials: Synthesis, properties, and applications. *Energy Environ. Sci.* **2012**, *5*, 8475–8505.
- (2) Ji, P.; Zhang, J.; Chen, F.; Anpo, M. Ordered mesoporous CeO₂ synthesized by nanocasting from cubic Ia3d mesoporous MCM-48 silica: Formation, characterization and photocatalytic activity. *J. Phys. Chem. C* **2008**, *112*, 17809–17813.
- (3) Yabe, S.; Sato, T. Cerium oxide for sunscreen cosmetics. *J. Solid State Chem.* **2003**, *171*, 7–11.
- (4) Hamdy, A. S. Advanced nanoparticles anti-corrosion ceria based sol gel coatings for aluminum alloys. *Mater. Lett.* **2006**, *60*, 2633–2637.
- (5) Marina, O. A.; Bagger, C.; Primdahl, S.; Mogensen, M. A solid oxide fuel cell with a gadolinia-doped ceria anode: preparation and performance. *Solid State Ionics* **1999**, *123*, 199–208.
- (6) Zhang, T. S.; Ma, J.; Chan, S. H.; Kilner, J. A. Grain boundary conduction of Ce_{0.9}Gd_{0.1}O_{2-δ} ceramics derived from oxalate coprecipitation: Effect of Fe loading and sintering temperature. *Solid State Ionics* **2005**, *176*, 377.
- (7) Sun, C.; Sun, J.; Xiao, G.; Zhang, H.; Qiu, X.; Li, H.; Chen, L. Mesoscale organization of nearly monodisperse flowerlike ceria microspheres. *J. Phys. Chem. B* **2006**, *110*, 13445–13452.
- (8) Pan, C.; Zhang, D.; Shi, L. CTAB assisted hydrothermal synthesis, controlled conversion and CO oxidation properties of CeO₂ nanoplates, nanotubes, and nanorods. *J. Solid State Chem.* **2008**, *181*, 1298–1306.
- (9) Tana; Zhang, M.; Li, J.; Li, H.; Li, Y.; Shen, W. Morphology-dependent redox and catalytic properties of CeO₂ nanostructures:

Nanowires, nanorods and nanoparticles. *Catal. Today* **2008**, *181*, 1298–1306.

(10) Sun, C.; Chen, L. Controllable of shuttle-shaped ceria and its catalytic properties for CO oxidation. *Eur. J. Inorg. Chem.* **2009**, *26*, 3883–3887.

(11) Sun, W. C.; Li, H.; Zhang, R. H.; Wang, X. Z.; Chen, Q. L. Controlled synthesis of CeO₂ nanorods by a solvothermal method. *Nanotechnology* **2005**, *16*, 1454–1463.

(12) Wang, Y.; Mori, N.; Li, J.; Ikegami, T. Low-temperature synthesis of praseodymium-doped ceria nanopowders. *J. Am. Ceram. Soc.* **2002**, *85*, 3105–3107.

(13) Araujo, V. D.; Avansi, W.; De Carvalho, H. B.; Moreira, M. L.; Longo, E.; Ribeiro, C.; Bernardi, M. I. B. CeO₂ nanoparticles synthesized by a microwave-assisted hydrothermal method: Evolution from nanospheres to nanorods. *CrystEngComm* **2012**, *14*, 1150–1154.

(14) Verma, A.; Karar, N.; Bakhshi, A. K.; Chander, H.; Shivaprasad, S. M.; Agnihotry, S. A. Structural morphological and photoluminescence characteristics of sol-gel derived nano phase CeO₂ films deposited using citric acid. *J. Nanoparticle Res.* **2007**, *9*, 317–322.

(15) Tsuzuki, T.; Robinson, J. S.; McCormick, P. G. UV-shielding ceramic nanoparticles synthesized by mechanochemical processing. *J. Aust. Ceram. Soc.* **2002**, *38*, 15–19.

(16) Guillo, N.; Nistor, L. C.; Fuess, H. Microstructural studies of nanocrystalline CeO₂ produced by gas condensation. *Nanostruct. Mater.* **1997**, *8*, 545–557.

(17) Welton, T. Room-temperature ionic liquids. Solvents for synthesis and catalysis. *Chem. Rev.* **1999**, *99*, 2071–2083.

(18) Hou, X.; Zhou, F.; Sun, Y.; Liu, W. Ultrasound-assisted synthesis of dendritic ZnO nanostructure in ionic liquid. *Mater. Lett.* **2007**, *61*, 1789–1792.

(19) Alammar, T.; Mudring, A.-V. Sonochemical synthesis of 0D, 1D, and 2D zinc oxide nanostructures in ionic liquids and their photocatalytic activity. *ChemSusChem* **2011**, *4*, 1796–1804.

(20) Alammar, T.; Birkner, A.; Shekhah, O.; Mudring, A.-V. Sonochemical preparation of TiO₂ nanoparticles in the ionic liquid 1-(3-hydroxypropyl)-3-methylimidazolium-bis-(trifluoromethylsulfonyl)amide. *Mater. Chem. Phys.* **2010**, *120*, 109–113.

(21) Alammar, T.; Mudring, A.-V. Facile ultrasound-assisted synthesis of ZnO in an ionic liquid. *Mater. Lett.* **2009**, *63*, 732–735.

(22) Alammar, T.; Mudring, A.-V. Ultrasound-assisted synthesis of CuO nanorods in a neat room temperature ionic liquid. *Eur. J. Inorg. Chem.* **2009**, *19*, 2765–2768.

(23) Mason, T. J.; Lorimer, J. P. *Sonochemistry: Theory Applications and Uses of Ultrasound in Chemistry*; Ellis Horwood Series in Physical Chemistry; Prentice Hall: Chichester, U.K., 1988

(24) Manickam, S. Sonochemical Synthesis of Oxides and Sulfides. In *Theoretical and Experimental Sonochemistry Involving Inorganic Systems*; Pankaj, M., Ashokkumar, Eds.; Springer: Heidelberg, 2011; pp 191–192.

(25) Branco, L. C.; Rosa, J. N.; Ramos, J. J. M.; Afonoso, C. A. M. Preparation and characterization of new room temperature ionic liquids. *Chem.-Eur. J.* **2002**, *8*, 3671–3677.

(26) Dubois, P.; Marchand, G.; Gmouh, S.; Vaultier, M. Reaction rates as a function of scale within ionic liquids: microscale in droplet microreactors versus macroscale reaction in the case of the Grieco three-component condensation reaction. *Chem.—Eur. J.* **2007**, *13*, 5642–5648.

(27) Noei, H.; Qiu, H.; Wang, Y.; Löffler, E.; Wöll, C.; Muhler, M. The identification of hydroxyl groups on ZnO nanoparticles by infrared spectroscopy. *Phys. Chem. Chem. Phys.* **2008**, *10*, 7092–7097.

(28) Wang, Y.; Glenz, A.; Muhler, M.; Wöll, C. A new dual-purpose ultrahigh vacuum infrared spectroscopy apparatus optimized for grazing-incidence reflection as well as for transmission geometries. *Rev. Sci. Instrum.* **2009**, *80*, 113108/1–113108/6.

(29) Vaqueiro, P.; Lopez-Quintela, M. A. Synthesis of yttrium aluminum garnet by the citrate gel process. *J. Mater. Chem.* **1998**, *8*, 161–163.

(30) Ayyub, A.; Palkar, V. R.; Chattopadhyay, S.; Multani, M. Effect of crystal size reduction on lattice symmetry and cooperative properties. *Phys. Rev. B* **1995**, *51*, 6135–6138.

(31) Goharshadi, K.; Samiee, S.; Nancarrow, P. Fabrication of cerium oxide nanoparticles: characterization and optical properties. *J. Colloid Interface Sci.* **2011**, *356*, 473–480.

(32) Wang, W.; Howe, J.; Li, Y.; Qiu, X.; Joy, D.; Paranthaman, M.; Doktycz, M.; Gu, B. A surfactant and template-free route for synthesizing ceria nanocrystals with tunable morphologies. *J. Mater. Chem.* **2010**, *20*, 7776–7781.

(33) Wang, G.; Mu, Q.; Chen, T.; Wang, Y. Synthesis characterization and photoluminescence of CeO₂ nanoparticles by a facile method at room temperature. *J. Alloys Compd.* **2010**, *493*, 202–207.

(34) Spanier, J.; Robinson, R.; Zhang, F.; Chan, S.-W.; Herman, I. Size-dependent properties of CeO₂-y nanoparticles as studied by raman scattering. *Phys. Rev. B* **2001**, *64*, 245407/1–245407/8.

(35) Araujo, V. D.; Avansi, W.; De Carvalho, H. B.; Moreira, M. L.; Longo, E.; Ribeiro, C.; Bernardi, M. I. B. CeO₂ nanoparticles synthesized by a microwave-assisted hydrothermal method: evolution from nanospheres to nanorods. *CrystEngComm* **2012**, *14*, 1150–1154.

(36) Reddy, B. M.; Reddy, G. K.; Reddy, L. H.; Ganesh, I. Synthesis of nanosized ceria-zirconia solid solutions by a rapid microwave-assisted combustion method. *Open. Phys. Chem. J.* **2009**, *3*, 24–29.

(37) Yan, B.; Zhu, H. Controlled synthesis of CeO₂ nanoparticles using novel amphiphilic cerium complex precursors. *J. Nanopart. Res.* **2008**, *10*, 1279–1285.

(38) Verma, A.; Bakhshi, S.; Agnihotry, S. Effect of different precursor sols on the properties of CeO₂-TiO₂ films for electrochromic window applications. *Electrochim. Acta* **2006**, *51*, 4639–4648.

(39) Burroughs, P.; Hamnett, A.; Orchard, A. F.; Thornton, G. Satellite structure in the X-ray photoelectron spectra of some binary and mixed oxides of lanthanum and cerium. *J. Chem. Soc., Dalton Trans.* **1976**, *17*, 1686–1698.

(40) Wolf, D.; Heber, M.; Grünert, W.; Muhler, M. Predictions of relationships between catalytic and solid phase properties by kinetic models and their validation. *J. Catal.* **2001**, *199*, 92–106.

(41) Shyu, J. S.; Weber, W. H.; Gandhi, S. H. Surface characterization of alumina-supported ceria. *J. Phys. Chem.* **1988**, *92*, 4964–4970.

(42) Salvi, A. M.; Varsano, F.; Speranza, G. Use of XPS for the study of cerium-vanadium (electrochromic) mixed oxides. *Surf. Interface Anal.* **2001**, *31*, 255–264.

(43) Reddy, B. M.; Reddy, G. K.; Ganesh, I.; Ferreira, J. M. Microwave-assisted Synthesis and structural characterization of nanosized Ce_{0.5}Zr_{0.5}O₂ for CO oxidation. *Catal. Lett.* **2009**, *130*, 227–234.

(44) Rogers, N. J.; Franklin, N. M.; Apte, S. C.; Batley, G. E.; Angel, B. M.; Lead, J. R.; Baalousha, M. Physico-chemical behaviour and algal toxicity of nanoparticulate CeO₂ in freshwater. *Environ. Chem.* **2010**, *7*, 50–60.

(45) Tsunekawa, S.; Fukuda, T.; Kasuya, A. Blue shift in ultraviolet absorption spectra of monodisperse CeO_{2-x} nanoparticles. *J. Appl. Phys.* **2000**, *87*, 1318–1321.

(46) Zhang, F.; Jin, S.-W.; Chan, Q. Ceria nanoparticles: Size, size distribution, and shape. *J. Appl. Phys.* **2004**, *95*, 4319–4326.

(47) Brus, L. E. Electron-electron and electron-hole interactions in small semiconductor crystallites: the size dependence of the lowest excited electronic state. *J. Chem. Phys.* **1984**, *80*, 4403–4409.

(48) Miao, J.-J.; Wang, H.; Li, Y.-R.; Zhu, J.-M.; Zhu, J.-J. Ultrasonic-induced synthesis of CeO₂ nanotubes. *J. Cryst. Growth* **2005**, *281*, 525–529.

(49) Morshed, A. H.; Moussa, M. E.; Bedair, S. M.; Leonard, R.; Liu, S. X.; El-Masry, N. Violet/blue emission from epitaxial cerium oxide films on silicon substrates. *Appl. Phys. Lett.* **1997**, *70*, 1647–1649.

(50) Zaki, M. I.; Vielhaber, B.; Knözinger, H. Low-temperature carbon monoxide adsorption and state of molybdena supported on alumina, titania, ceria, and zirconia. an infrared spectroscopic investigation. *J. Phys. Chem.* **1986**, *90*, 3176–3183.

- (51) Wang, Y.; Xia, X.; Urban, A.; Qiu, H.; Strunk, J.; Meyer, B.; Muhler, M.; Wöll, C. Tuning the reactivity of oxide surfaces by charge-accepting adsorbates. *Angew. Chem., Int. Ed.* **2007**, *46*, 7315–7319.
- (52) Noei, H.; Wöll, C.; Muhler, M.; Wang, Y. The interaction of carbon monoxide with clean and surface-modified zinc oxide nanoparticles. A UHV-FTIRS study. *Appl. Catal., A* **2011**, *391*, 31–35.
- (53) Elidrissi, B.; Addou, M.; Regragui, M.; Monty, C.; Bougrine, A.; Kachouane, A. Structural and optical properties of CeO₂ thin films prepared by spray pyrolysis. *Thin Solid Films* **2000**, *379*, 23–27.
- (54) Palmqvist, A. E. C. Synthesis of ordered mesoporous materials using surfactant liquid crystals or micellar solutions. *Curr. Colloid. Interface Sci.* **2003**, *8*, 145–155.
- (55) Cao, X.; Wang, N.; Wang, L.; Guo, L. Porous ZnO nanobelts: Synthesis, mechanism, and morphological evolutions. *J. Nanopart. Res.* **2010**, *12*, 143–150.
- (56) Yuejuan, W.; Jingmeng, M.; Mengfei, L.; Ping, F.; Mai, H. Preparation of high-surface area nano-CeO₂ by template-assisted precipitation method. *J. Rare. Earths* **2007**, *25*, 58–62.
- (57) Handy, S. T. *Ionic Liquids—Classes and Properties*; InTech: Rijeka, Croatia, 2011.
- (58) Alammar, T.; Noei, H.; Wang, Y.; Mudring, A.-V. Mild yet phase-selective preparation of TiO₂ nanoparticles from ionic liquids: A critical study. *Nanoscale* **2013**, *5*, 8045–8055.
- (59) Klabunde, K. J.; Richards, R. M. *Nanoscale Materials in Chemistry*; John Wiley & Sons, Inc: New York, 2009; pp 205.
- (60) Stepnowski, P. ¹³C NMR Relaxation Studies of Ionic Liquids. In *Ionic Liquids IV: Not Just Solvents Anymore*; Brennecke, J. F., Rogers, R. R., Seddon, K. R., Eds.; ACS Symposium Series 975; American Chemical Society: Washington, DC, **2007**; pp 11–12.
- (61) Ott, L. S.; Cline, M. L.; Deetlefs, M.; Seddon, K. R.; Finke, R. G. Nanoclusters in ionic liquids: Evidence for N-heterocyclic carbene formation from imidazolium-based ionic liquids detected by ²H NMR. *J. Am. Chem. Soc.* **2005**, *127*, 5758–5759.
- (62) Wittmar, A.; Gajda, M.; Gautam, D.; Dörfler, U.; Winterer, M.; Ulbricht, M. Influence of the cation alkyl chain length of imidazolium-based room temperature ionic liquids on the dispersibility of TiO₂ nanopowders. *J. Nanopart. Res.* **2013**, *15*, 1463–1475.
- (63) Han, L.; Liu, R.; Li, C.; Li, H.; Li, C.; Zhang, G.; Yao, J. Controlled synthesis of double-shelled CeO₂ hollow spheres and enzyme-free electrochemical bio-sensing properties for uric acid. *J. Mater. Chem.* **2012**, *22*, 17079–17085.
- (64) Miao, S.; Liu, Z.; Miao, Z.; Han, B.; Ding, K.; An, G.; Xie, Y. Ionic liquid-mediated synthesis of crystalline CeO₂ mesoporous films and their application in aerobic oxidation of benzyl alcohol. *Microporous Mesoporous Mater.* **2009**, *117*, 386–390.
- (65) Li, Z.-X.; Li, L.-L.; Yuan, Q.; Feng, W.; Xu, J.; Sun, L.-D.; Song, W.-G.; Yan, C.-H. Sustainable and facile route to nearly monodisperse spherical aggregates of CeO₂ nanocrystals with ionic liquids and their catalytic activities for CO oxidation. *J. Phys. Chem. C* **2008**, *112*, 18405–18411.
- (66) Zhou, K.; Wang, X.; Sun, X.; Peng, Q.; Li, Y. Enhanced catalytic activity of ceria nanorods from well-defined reactive crystal planes. *J. Catal.* **2005**, *229*, 206–212.
- (67) Wu, Z.; Li, M.; Overbury, S. H. On the structure dependence of CO oxidation over CeO₂ nanocrystals with well-defined surface planes. *J. Catal.* **2012**, *285*, 61–73.